

Ion transport in helical-helical polypeptide polymerized ionic liquid block copolymers

Received: 14 October 2024

Accepted: 4 March 2025

Published online: 12 March 2025

Yingying Chen¹, Tianjian Yang², Yao Lin² & Christopher M. Evans¹✉

Helical-helical polypeptide polymerized ionic liquid block copolymers (PPIL BCPs) are synthesized to investigate the role of helical structure on self-assembly and ionic conductivity. PPIL BCPs, consisting of a cationic polypeptide (PTPLG) with bis(trifluoromethane sulfonimide) (TFSI) counterion and varying lengths connected to a length-fixed neutral poly-(γ -benzyl-L-glutamate) (PBLG) block, exhibit stable helical conformations with minimal glass transition (T_g) variation. Here, we show that increasing PIL composition leads to a transition from poorly ordered to highly ordered lamellar (LAM) structures with the highest PIL content BCP forming a bilayer LAM structure with close-packed helices. This morphology yields a 1.5 order of magnitude higher T_g - and volume fraction-normalized ionic conductivity and a morphology factor $f > 0.8$ compared to less ordered BCPs with $f < 0.05$ and $f = 2/3$ for ideal lamellae. These results highlight the critical role of helical structure in optimizing ion transport, offering a design strategy for high-performance solid electrolytes.

Ion transport in polymers is an important concept for improving solid state energy storage devices like batteries. Polymerized ionic liquids (PILs), which feature bulky ionic liquid groups tethered to polymer backbones, represent a promising advance in the field of ion conducting polymers^{1–7}. PILs exhibit a unique combination of chemical and physical properties including high single ion conductivity, thermal and electrochemical stability, and selectivity and mechanical tunability making them attractive in applications such as energy storage systems^{8–10}, separation media^{11,12}, catalysis^{13,14} and antimicrobial^{15,16}. Various architectures including linear¹⁷, block^{18–20} and network^{21–23} PILs have been investigated to improve conductivity, stability and mechanical integrity. Among these, block copolymers (BCPs) are particularly promising due to their ability to create nanoscale morphologies, and many factors can significantly affect the ionic conductivity of PIL BCP systems, including molecular weight, neutral block chemistry, doping with other components, tortuosity, volume fraction (ϕ_{PIL}) of ionic block, and nanoconfinement^{24–34}. Conductivity can increase, decrease, or be invariant in a PIL diblock relative to the corresponding homopolymer. BCPs allow for the separate design of each block to provide complementary functionality between ionic transport and structural properties. PIL BCPs demonstrate a range of phase

separation strength depending on the non-ionic block, which impacts the degree of confinement and ordering of ion-conducting channels, which affect ion transport. While PIL BCPs have shown great promise, the use of polymers with more ordered backbone structures (such as peptides) compared to the current random coil configurations has not been explored.

In previous work, Chen et al. developed a series of cationic polypeptides (PTPXGs) with a fixed ionic monomer structure but different secondary structures, either helical or random coil depending on the chirality of the monomer. The tethered ion was ammonium with free bis (trifluoromethane sulfonimide) (TFSI) and peptides varied from 50–950 repeating units. The helical structure greatly enhanced the ionic conductivity and thermal stability of solvent-free polymer electrolytes compared to analogous random coils, and conductivity increased with helix length³⁵. The critical role of helical backbone on charge transport introduces a distinct parameter to the design of polymer electrolytes, and has also been shown to improve electron transport either with attached stable radical groups³⁶ or through tunneling in monolayers³⁷. The role of helical structure in solvent-free PIL BCPs is unexplored, both in terms of self-assembly and conductivity, in contrast to the many works on random coil polymer backbones. Rigid

¹Department of Materials Science and Engineering, Materials Research Laboratory, University of Illinois Urbana-Champaign, Urbana, IL, USA. ²Department of Chemistry, University of Connecticut, Storrs, CT, USA. ✉ e-mail: cme365@illinois.edu

rod chains exhibit distinct aggregation behavior and intramolecular interaction compared to coils, and the self-assembly of rod-coil BCPs deviates from that of conventional coil-coil systems^{38,39}. The predicted critical value of $(\chi N)_c$ for rod-rod and coil-coil BCPs are 8.2 and 10.5 (where χ is the Flory-Huggins interaction parameter, N is the total degree of polymerization), respectively⁴⁰. Rigid rod polymers can be tuned in terms of shapes and size and leads to the formation of three-dimensional assemblies^{41–43}, such as superlattices and liquid crystal (LC) phases. Peptides derived from *N*-carboxyanhydride (NCA) ring-opening polymerizations (ROP) are ideal rod-like ionic blocks because they can be readily synthesized to high molecular weight compared to solid-phase synthesis approaches. The helical blocks can self-assemble in PIL block copolymers and offer distinct nanoscale morphologies compared to random coils. Incorporation of helical peptide backbones into neutral BCPs can promote ordered nanostructures within the BCP matrix and has been investigated for creating functional materials with supramolecular architectures^{44–49}. Ionic peptides have the potential to substantially impact ion transport and self-assembly, and PIL BCPs with helical ionic blocks provide an additional design parameter for polymer electrolytes.

In this study, helical-helical polypeptide PIL BCPs (PPIL BCPs) composed of an ionic poly(γ -3-triazolepropyl-L-glutamate) (PTPLG) and non-ionic poly(γ -benzyl-L-glutamate) (PBLG) block were synthesized. The role of helical structure on self-assembly and ion conduction was studied by varying the ionic block degree of polymerization ($N=15, 30$, and 75) while keeping the non-ionic PBLG block length constant ($N=30$). Strong microphase separation slightly lowered the glass transition temperature (T_g) of BCPs with higher PIL composition, although only one glass transition was observed due to the proximity of the two block T_g s. Hot-pressed films exhibited similar lamellar structure (LAM) with varying domain sizes (d) and degrees of order, as determined by small-angle X-ray scattering (SAXS). A more than 1.5 order of magnitude higher T_g -normalized and ϕ_{PIL} -normalized ionic conductivity was observed in PBLG₃₀-*b*-PTPLG₇₅ with a highly ordered

bilayer LAM phase compared to less ordered structures, highlighting the importance of confinement, helix length, and nanoscale ionic domain connectivity. Furthermore, a morphology factor of $f > 0.8$ in PBLG₃₀-*b*-PTPLG₇₅ (above the theoretical value of $2/3$ for lamellae) was achieved throughout the entire temperature window, indicating enhanced ion transport channels. Interestingly, these channels become more effective at low temperatures, as evidenced by f values greater than 1 below 65°C . This study provides creative insights into the critical role of helical conformation in both self-assembly behavior and ionic conductivity of peptide electrolytes, providing directions for future study on structure–property relationships and the design of functional assemblies with well-defined size for next-generation stable and high-performance electrolytes.

Results and discussion

Construction of helical PPIL BCPs

The PPIL BCPs were derived from precursors with PBLG and poly(γ -3-chloropropyl)-L-glutamate (PCIPLG) blocks synthesized using sequential ROPs. A series of PBLG₃₀-*b*-PCIPLG_{*n*} BCPs was prepared starting with a non-ionic helical PBLG-NH₂ macroinitiator prepared by ROP of γ -benzyl-L-glutamate NCA (BLG-NCA, Supplementary Fig. 1) using *n*-hexylamine as initiator in *N,N*-dimethylformamide. Next, PBLG-NH₂-initiated ROP of γ -(3-chloropropyl)-L-glutamate NCA (CIPLG-NCA) in dichloromethane/phosphate buffer emulsion system ($V_{\text{DCM}}/V_{\text{pH 7 buffer}} = 95\%/5\%$) ($[\text{NCA}]_0 = 50\text{ mM}$, Fig. 1) was performed. The N of PBLG-NH₂ was fixed at 30 to ensure the formation of a stable α helix (Supplementary Fig. 2)⁵⁰. Successful BCP precursor synthesis was confirmed by size exclusion chromatography (SEC, Fig. 2a) and ¹H NMR to determine molecular weight (M_n). Attenuated total reflectance-Fourier transform infrared spectra (ATR-FTIR) was used to confirm the presence of helical conformation in the solid state. Controlled NCA-ROPs led to BCP precursors with well-defined length and low dispersity ($\bar{D} < 1.1$) (Supplementary Table 1). The M_n of PBLG-NH₂ ($M_n = 6.83\text{ kDa}$) and PBLG₃₀-*b*-PCIPLG_{*n*} ($M_n = 9.12, 13.53$ and 22.57 kDa)

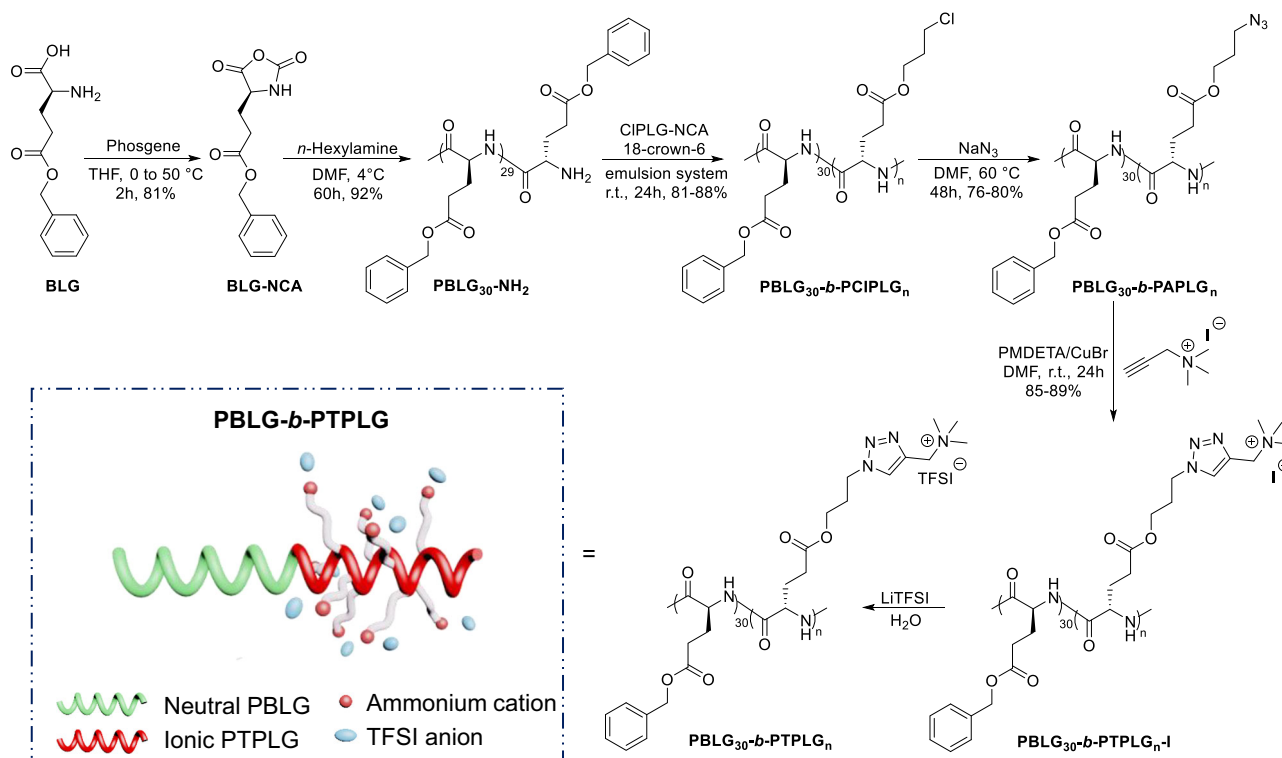


Fig. 1 | Synthesis of helical PPIL BCPs by ring opening polymerization. Synthesis route for PBLG₃₀-*b*-PTPLG_{*n*} PPIL BCPs includes NCA formation, ring opening polymerization, chain extension, azidation, click chemistry, and anion exchange.

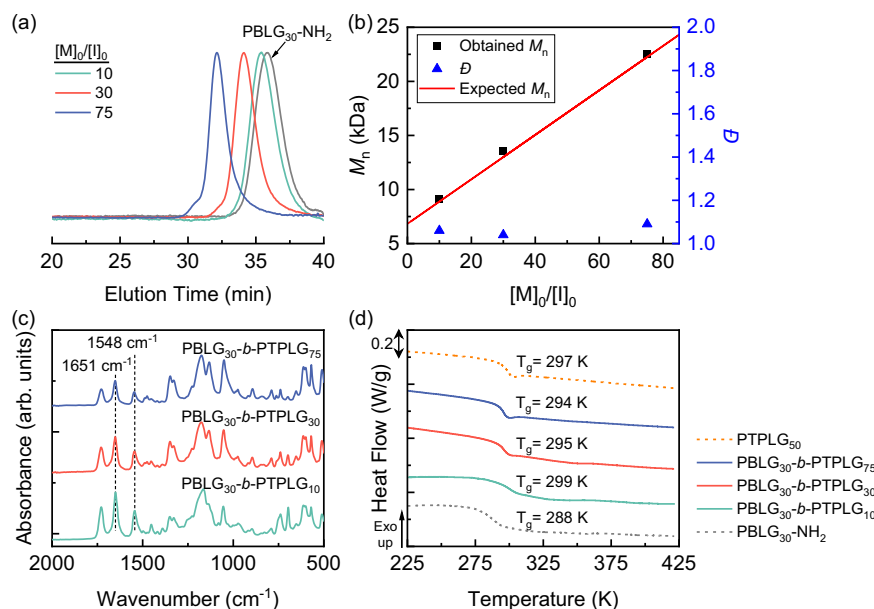


Fig. 2 | Characterization of molecular weight, helical secondary structure, and glass transition temperatures. **a** Normalized SEC-LS traces of α -helical macro-initiator PBLG₃₀-NH₂ (gray) produced by hexylamine-initiated ROP of BLG-NCA in DMF and BCP precursors PBLG₃₀-b-PCIPLG_ns synthesized by PBLG₃₀-NH₂-initiated ROP of CIPLG-NCA in emulsion system ($V_{\text{DCM}}/V_{\text{pH}=7 \text{ phosphate buffer}} = 95\% / 5\%$) with

different feeding ratios $[M]_0/[I]_0$. **b** Comparison of the expected MWs, obtained MWs and \bar{D} of PBLG₃₀-b-PCIPLG_ns. **c** ATR-FTIR spectra indicating the characteristic amide I peak. **d** Second heat cycle DSC curves of PBLG₃₀-b-PTPLG_ns and homopolymers.

as determined by SEC aligned well with the theoretical M_n and those calculated from ¹H NMR end group analysis (Fig. 2b). The n values and mole fraction (mol %) of PBLG₃₀-b-PCIPLG_ns were calculated from the integral ratio of the proton on the central carbon of each block (4.95 and 5.05 ppm, respectively) in ¹H NMR spectra (Supplementary Figs. 2–5). Azidation, copper-catalyzed azide–alkyne cycloaddition (CuAAC) click reactions and salt metatheses were employed to produce the final PPIL BCPs named PBLG₃₀-b-PTPLG_ns, where positively charged ammonium groups are fixed on the end of side chain while bis(trifluoromethane) sulfonamide (TFSI) counterions remain mobile within the ionic block (Fig. 1). The final composition (n and mol %) after functionalization was confirmed by ¹H NMR to be consistent with that of the corresponding precursors (Supplementary Fig. 6). Three PPILs BCPs (PBLG₃₀-b-PTPLG₁₀, PBLG₃₀-b-PTPLG₃₀ and PBLG₃₀-b-PTPLG₇₅) with fixed non-ionic block length ($N=30$) but varying ionic block length ($N=10, 30$, and 75 , respectively) were obtained, as well as two homopolymers, PBLG₃₀ and PTPLG₅₀. All polymers were dried in a vacuum oven and stored in a glove box before use.

Conformation and thermal properties of PPIL-BCPs

The secondary structures of the PPIL BCPs in the solid-state were evaluated by ATR-FTIR and circular dichroism (Fig. 2c, Supplementary Fig. 7). As anticipated, all block copolypeptides exhibited a right-handed α -helical conformation, as a result of the strong α -helix formation tendency of each block within the appropriate N range ($N \geq 19$ is required for the formation of α -helical PBLG⁵⁰). The characteristic absorbance peaks of amide I at 1651 cm⁻¹ and amide II at 1548 cm⁻¹ are observed for all BCPs. The absence of peaks corresponding to the random coil at 1660 cm⁻¹ indicates that both blocks predominantly adopt an α -helical conformation in PPIL BCPs. Furthermore, the helical secondary structures displayed stability across the whole temperature range investigated (25 to 140 °C), as evidenced by the invariance of absorption peak of amide I in temperature-dependent FTIR spectra (Supplementary Fig. 8).

Thermal gravimetric analysis and differential scanning calorimetry (DSC) were used for the evaluation of their thermal properties.

All PPIL BCPs showed similar degradation temperature (T_d , determined as 5% mass loss, Supplementary Fig. 9, Supplementary Table 2). Figure 2d shows the glass transition temperatures (T_g s) of three PPIL BCPs in comparison to the two homopolymers (Supplementary Fig. 10). Only a single T_g was observed in all BCPs, likely due to the relatively small T_g difference (10 K) between the two blocks ($T_{g, \text{PBLG}} = 288 \text{ K}$ and $T_{g, \text{PTPLG}} = 298 \text{ K}$) and compatible nature of peptide backbones. A single T_g does not imply the absence of microphase separation that typically manifests as two distinct T_g s corresponding to the ionic block and non-ionic block, respectively⁵¹, and clear microphase separation was confirmed by SAXS. The T_g of the helical PPIL BCPs only slightly decreased with significantly increasing PIL composition. Specifically, for PBLG₃₀-b-PTPLG₃₀ and PBLG₃₀-b-PTPLG₇₅ the T_g decreased negligibly from 295 to 294 K as the PIL composition increases from 50 to 71 mol %. It was observed that PBLG₃₀-NH₂ exhibited the broadest glass transition, and as the PIL mol % increased the glass transition narrowed, reaching the smallest breadth in homo-PTPLG₅₀. The narrowing of T_g is also consistent with strong microphase separation in BCPs.

Morphology of helical PPIL BCPs

SAXS was used to explore the self-assembly behavior of helical–helical PPIL BCPs. All samples were hot-pressed into self-standing films at 80 °C with 1.5 tons for 5 min and then annealed at 140 °C for 4 h to enhance the ordering and form stable morphologies (Supplementary Fig. 11). PBLG₃₀-b-PTPLG_ns all showed well-defined structures (Fig. 3a). Strong microphase separation with long range periodicity was confirmed by multiple reflections. All BCPs exhibited LAM structures, though significant differences in domain spacings (d , the center-to-center distance between adjacent non-ionic or ionic lamellae) and the degree of order varied with PIL mol%. At a fixed N of the PBLG block, the increase of PIL block length led to larger d and more ordered LAM morphologies as expected for increased N and χN . Notably, PBLG₃₀-b-PTPLG₇₅ displayed up to seven clear reflections at $q^*, 2q^*, 3q^*, 4q^*, 5q^*, 6q^*$, and $7q^*$ (with q^* as the primary peak position, $q^* = 0.019 \text{ \AA}^{-1}$), indicating a highly ordered LAM morphology with $d = 33 \text{ nm}$

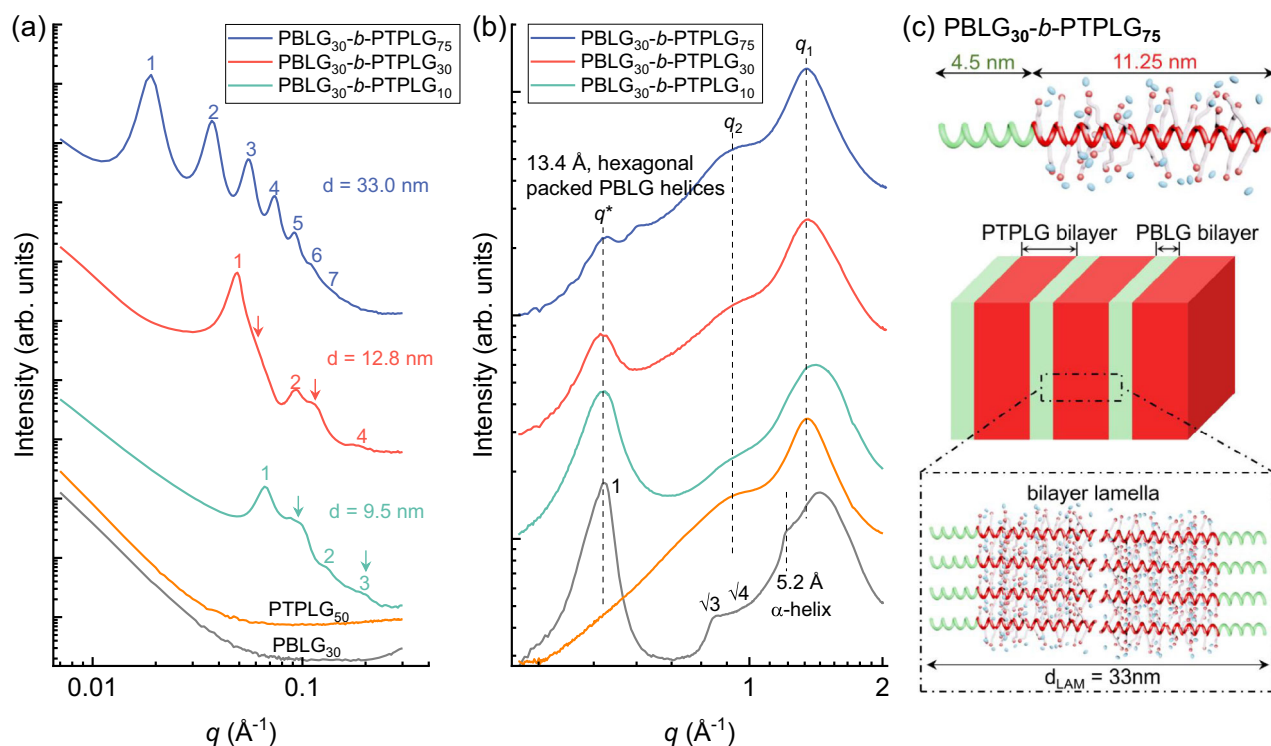


Fig. 3 | Microphase separation of helical PPIL BCPs films. **a** SAXS and **b** WAXS profiles of PBLG₃₀-b-PTPLG_ns annealed hot-pressed films, compared to two homopolymers. **c** Schematic representation of head-to-head bilayer lamella structure of PBLG₃₀-b-PTPLG₇₅. Top: the theoretical polymer length calculated based on

a helical pitch of 0.54 nm. Middle: overall block copolymer structure. Bottom: the packing scheme of two blocks in their respective domains. PBLG and PTPLG are indicated by green and red colors, respectively.

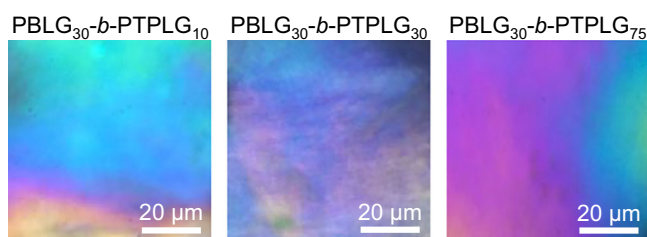
(calculated by $d = 2\pi/q^*$). The LAM structures formed by rod-rod BCP self-assembly can be further classified as single-layer, interdigitated, or bilayer structures, depending on the specific packing arrangement of the helices^{43,52}. To better understand the packing of each helical block within microphase-separated layers, the 18/5 helix model (α -helical conformation of 18 residues in 5 turns) with a helical pitch of 0.54 nm was applied⁵³, where the helical backbone length L_{helix} (nm) = $N \times 0.15$ nm. For PBLG₃₀-b-PTPLG₇₅ where $d \approx 2L$, the theoretical calculated length of $L = 15.75$ nm ($L_{\text{PBLG}} = 4.5$ nm and $L_{\text{PTPLG}} = 11.25$ nm) was compared to the measured $d = 33$ nm from SAXS corresponding to a bilayer lamella structure with both blocks arranged in a head-to-head bilayer conformation (Fig. 3c). PPIL BCPs with lower PIL mol % exhibited poorly ordered LAM structure likely due to the disrupted balance between the molecular packing of two helical blocks with different cylindrical size, as indicated by the coexistence of two distinct interdigitated LAM with different domain spacings (Supplementary Fig. 12). In PBLG₃₀-b-PTPLG₃₀ ($L = 9$ nm), one set of scattering peaks at q^* , $2q^*$, and $4q^*$ ($q^* = 0.049 \text{ \AA}^{-1}$) corresponds to a partially interdigitated LAM morphology with $d = 12.8$ nm. A second set of peaks located between $q^* - 2q^*$ and $2q^* - 4q^*$ (indicated by arrows) with a ratio of 1:2 ($q \sim 0.06 \text{ \AA}^{-1}$) suggests another interdigitated LAM structure with $d \approx 10.4$ nm, where both helical blocks packed in an interdigitated manner. Similarly, PBLG₃₀-b-PTPLG₁₀ ($L = 6$ nm) with the shortest PIL block also showed a mixed LAM structure evidenced by two sets of scattering peaks. The dominant LAM structure had a d spacing of 9.5 nm, characterized by peaks at q^* , $2q^*$, and $3q^*$ ($q^* = 0.066 \text{ \AA}^{-1}$). Likely, the PBLG₃₀ blocks were organized into a bilayer structure while the PTPLG₁₀ blocks adopt an interdigitated packing. The shoulder peak (arrow, $q = 0.092 \text{ \AA}^{-1}$, $d = 6.8$ nm) suggests the coexistence of another phase with interdigitated packing in both the PBLG and PTPLG domains. The coexistence of two interdigitated LAM morphologies reflects the overall less ordered structure in PBLG₃₀-b-PTPLG₃₀ and PBLG₃₀-b-PTPLG₁₀ compared to PBLG₃₀-b-PTPLG₇₅. Previous studies

on rod-rod BCP systems have attributed limited overall LAM order to rod diameter disparity⁵³ or packing periodicity mismatch⁵⁴, with defects mitigated by increasing volume fraction of large diameter blocks or incorporating β -sheet conformations that are more compatible with LAM packing⁵⁵. The transition from weakly ordered to highly defined LAM structures in our system aligns with the former explanation, as the ϕ_{PIL} of the larger diameter block PIL (Table 1) increased from 43.2% in PBLG₃₀-b-PTPLG₁₀ to 85.1% in PBLG₃₀-b-PTPLG₇₅. Additionally, Banno et al. observed that head-to-head bilayer packing collapses when the overall helical length increased from ~ 17 to 34 nm in their helical rod-rod polyisocyanide BCPs⁴³. Thus, a specific length of PTPLG block is required in our PPIL BCPs to achieve a highly ordered bilayer structure.

Wide-angle X-ray scattering (WAXS) was employed to investigate both the peptide secondary structure and confinement effects for the ionic groups in bulk films. As shown in Fig. 3b, the characteristic reflections of PTPLG helix-helix correlations were absent, likely resulting from the ionic interactions of ammonium-TFSI ion pairs and complex side-chain packing that disrupt interhelix interactions. The steric effects of bulky ionic groups and anion-anion aggregation weaken the long-range packing of the PTPLG helices. However, reflections with ratios of 1: $\sqrt{3}$: $\sqrt{4}$, relative to the primary peak $q^* = 0.47 \text{ \AA}^{-1}$ in a PBLG film indicates 2D hexagonal packing of cylinders composed of 18/5 helices with a cylinder spacing of 13.4 Å. This primary peak was present in all BCPs, suggesting that the PBLG segments were organized in a similar way in the BCPs, which provided the driving force for segregating the PTPLG blocks into LAM structures. The absence of long-range orders in PTPLG likely leads to a more disordered structure within its lamellar domains. The diffraction peak with a spacing of 5.2 Å corresponds to the layer line spacing of the PBLG helix⁵⁶. Additionally, two other scattering peaks were observed. The highest peak (q_1) was assigned as the amorphous halo corresponding to the backbone correlations, while the intermediate peak

Table 1 | PBLG₃₀-*b*-PTPLG_{*n*} physical properties and VFT fit parameters for temperature-dependent ionic conductivities

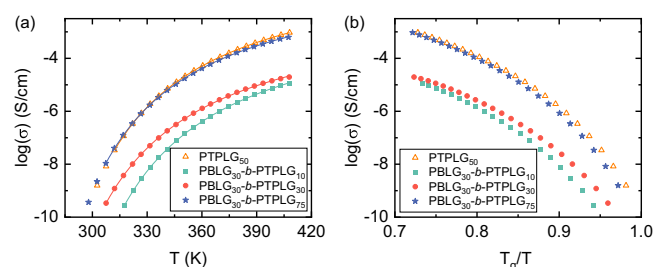
Polymers ^a	mol ^b (%)	ϕ_{PIL}^c (%)	T_g^d (K)	T_o^e (K)	$T_g - T_o^e$ (K)	σ_∞^e (S/cm)	D^e	L^f (nm)	d^g (nm)	f
PBLG ₃₀	0	0	289	/	/	/	/	4.5	/	0
PBLG ₃₀ - <i>b</i> -PTPLG ₁₀	25	43.2	299	255	44	0.02	4.48	6	9.5	<0.03
PBLG ₃₀ - <i>b</i> -PTPLG ₃₀	50	69.5	295	246	49	0.018	4.41	9	12.8	<0.05
PBLG ₃₀ - <i>b</i> -PTPLG ₇₅	71	85.1	294	248	46	0.41	4.15	15.8	33.0	>0.8
PTPLG ₅₀	100	100	298	249	48	0.73	4.27	7.5	/	1

^aSubscripts denote the *N* of each block in PPIL BCPs via ¹H NMR in TFA-*d*.^bMole fraction of ionic PTPLG block, determined by quantitative ¹H NMR.^cVolume fraction of PTPLG block determined by the $\rho_{\text{PBLG}} = 1.28 \text{ g/cm}^3$ (Zhou et al.⁵²) and $\rho_{\text{PTPLG}} = 1.51 \pm 0.04 \text{ g/cm}^3$ (determined by pycnometer, data are means \pm s.d., *n* = 3 independently replicates, see Supplementary Information for details).^dDetermined by DSC of hot-pressed film samples.^eDetermined by Vogel–Fulcher–Tammann (VFT) fitting parameters.^fTheoretical length of PPIL BCPs, calculated based on the 18/5 α -helical model with a helical pitch of 0.54 nm.^gDetermined by SAXS using the position of the primary peak.**Fig. 4 | LC-like ordering of PPIL BCPs hot-pressed films.** Polarized optical micrographs of helical-helical PBLG₃₀-*b*-PTPLG_{*n*} hot-pressed films annealed at 140 °C.

(q_2) reflects the correlation of the TFSI anion^{57,58}. The non-ionic PBLG showed the broadest amorphous peak at $q_1 \sim 1.44 \text{ \AA}^{-1}$ while ionic PTPLG exhibited the narrowest peak with a significant shift to $q_1 \sim 1.35 \text{ \AA}^{-1}$. The intensity of q_2 peaks increased with PIL mol% (Supplementary Fig. 13), indicating that higher PIL compositions lead to stronger ion–ion correlations. The q_2 peak of PBLG₃₀-*b*-PTPLG₇₅ ($q_2 = 0.97 \text{ \AA}^{-1}$) was slightly shifted to a larger q value compared to homo-PTPLG ($q_2 = 0.94 \text{ \AA}^{-1}$), possibly due to the highly ordered bilayer LAM structure, which causes TFSI anions to pack more efficiently within the ionic domain. This increased intensity and q_2 value enhanced the ionic conductivity as discussed later.

Helical polypeptides can form a range of LC structures⁵⁹. Polarized optical microscopy (POM) revealed birefringent textures in PBLG₃₀ and PBLG₃₀-*b*-PTPLG_{*n*} hot-pressed films (same samples used in SAXS/WAXS measurements), indicating the presence of LC-like ordering (Fig. 4 and Supplementary Fig. 14)⁴⁹. All PPIL BCPs were heated on the POM to 150 °C, more than 120 °C above their T_g s, and retained the iridescence textures (Supplementary Fig. 15). For the ionic PTPLG block, no iridescence was observed for *N* = 50 and a longer helical backbone was required to induce ordering which was confined to the surface of hot-pressed films³⁵. The incorporation of a PBLG block enhances the LC-like ordering of PTPLG in BCPs.

Ionic conductivity of PPIL BCPs. Figure 5a presents the temperature-dependent ionic conductivity of PBLG₃₀-*b*-PTPLG_{*n*}s with varying PIL composition compared to that of homo-PTPLG₅₀ and the non-ionic precursor (Supplementary Fig. 16) over a temperature range of 25 to 140 °C, with a cooling rate of 5 °C/h. A non-Arrhenius conductivity was observed as expected for polymers with tethered ionic groups^{7,57,60–63}. Consistent with previous studies on PIL BCPs where the ionic conductivity typically increases with higher PIL mol %^{30,31}, PBLG₃₀-*b*-PTPLG₇₅ with the highest PIL composition (71 mol %) exhibited the highest ionic conductivity. This conductivity is comparable to that of

**Fig. 5 | Higher PIL composition promotes conductivity.** **a** Temperature-dependent ionic conductivity of PBLG₃₀-*b*-PTPLG_{*n*}s, compared with homopolymer PTPLG₅₀. Solid lines are VFT fits. **b** T_g -normalized ionic conductivity.

homo-PTPLG, 1–2 orders of magnitude higher than that of PBLG₃₀-*b*-PTPLG₃₀ (50 mol %), and nearly 2 orders of magnitude higher than PBLG₃₀-*b*-PTPLG₁₀ (25 mol %). The ionic conductivity of PBLG₃₀-*b*-PTPLG₃₀ and PBLG₃₀-*b*-PTPLG₁₀ converge at higher temperatures, while PBLG₃₀-*b*-PTPLG₃₀ and PBLG₃₀-*b*-PTPLG₇₅ exhibit similar behavior at lower temperatures. This variation in temperature dependence of ionic conductivity with different PIL mol % is attributed to confinement effects within the block copolymer domains, which influences the morphology of ion aggregates, thereby affecting conductivity⁶⁴. This correlation is supported by the changes in the position and intensity of the q_2 peaks observed in WAXS (Supplementary Fig. 13).

To investigate the temperature-related ion conduction behavior of our PPIL BCPs, ionic conductivities at $T_g + 10 \text{ K}$ and above were fit with the VFT equation (solid line in Fig. 5a):

$$\sigma(T) = \sigma_\infty \exp\left(-\frac{DT_0}{T - T_0}\right) \quad (1)$$

where σ_∞ , D , and T_0 are the limiting high temperature ionic conductivity before degradation, the strength parameter, and the Vogel temperature where the ionic conductivity hypothetically diverges to zero. Fit parameters are summarized in Table 1. The hypothetical high temperature conductivity (σ_∞) of PBLG₃₀-*b*-PTPLG₇₅ was observed to be more than 20-fold than that of the PBLG₃₀-*b*-PTPLG₁₀ and PBLG₃₀-*b*-PTPLG₃₀, corresponding to an increase of the overall ionic content. Notably, all T_0 values are consistently lower than their T_g s by around 45 K, which is similar to other PIL systems particularly those with rigid backbones⁶³. The strength parameters (D) is also one factor relating to decoupling of conductivity from segmental dynamics, with lower D generally corresponding to higher conductivities at a given distance from T_g ⁶⁵. All PPIL BCPs exhibited similar D values, with a slight decrease in D with increasing PIL content. To gain further insight into the role of segmental dynamics, T_g -normalized ionic conductivity was

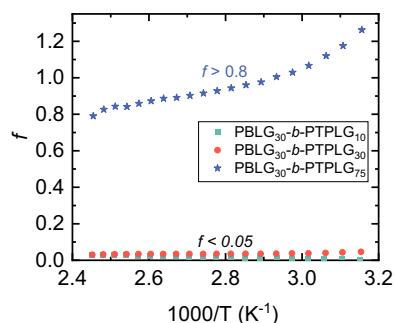


Fig. 6 | Highly ordered bilayer lamellar structure enables higher morphology factor. Morphology factor f of PBLG₃₀-*b*-PTPLG_ns with different ionic block composition as a function of temperature.

also plotted and shown in Fig. 5b. PBLG₃₀-*b*-PTPLG₇₅ maintained overlap with homo-PTPLG despite a lower overall ionic content. This BCP also showed an ~ 1.5 – 2 order of magnitude higher conductivity than PBLG₃₀-*b*-PTPLG₁₀ and PBLG₃₀-*b*-PTPLG₃₀. The T_g -normalized ionic conductivity difference between PBLG₃₀-*b*-PTPLG₁₀ and PBLG₃₀-*b*-PTPLG₃₀ diminished at higher temperature and merge in a mol %-normalized conductivity indicating the ionic content is controlling this regime (Supplementary Fig. 17). Despite all PPIL BCPs displaying similar T_g , T_0 and D values, significant differences in conductivities were observed and attributed to the distinct nanostructures and degree of order. An independent set of all PPIL BCPs were prepared and displayed reproducible conductivity (Supplementary Fig. 18 and Supplementary Table 3).

Interestingly, the ionic conductivity at fixed temperature increases non-linearly with increasing PIL mol %. Specifically, a more than 1.5 order of magnitude increase in ionic conductivity was achieved across the entire temperature range when the PIL composition increased from 50 to 71 mol %. More specifically, the ionic conductivity increased from 0.02 mS/cm to 0.71 mS/cm at 408 K. While increasing PIL content from 25 to 50 mol % led to a difference of 2 to 13-fold with decreasing temperature, with the largest conductivity enhancement of 2.7×10^{-4} to 3.7×10^{-3} μ S/cm at 318 K. No discernible conductivity increase can be observed between 71 and 100 PIL mol %. This non-linear correlation between conductivity and composition of ionic block has been noted in other PIL BCP systems as well^{30,31} and attributed to morphological effects. The ionic conductivity was significantly increased when the morphology changes from 1-D hexagonally packed cylinders to a lamellar structure that can provide 2D pathways to facilitate ion transport. Conductivity was further increased in morphologies with percolated 3D pathways.

The PPIL BCPs were further analyzed using the morphology factor (f) to normalize the ion conductivity (Fig. 6):

$$f = \frac{\sigma}{\phi_c \sigma_c} \quad (2)$$

where σ is the measured ionic conductivity of PIL BCPs, ϕ_c , and σ_c are the volume fraction and intrinsic ionic conductivity of the pure PIL block, respectively. Typically, theoretical f values (f_{ideal}) for PIL BCP solid electrolytes are $1/3$, $2/3$, and 1 , corresponding to randomly oriented domains of 1-D hexagonally packed cylinders, 2D lamella, and 3D networks, respectively. However, experimental values often fall short of these values^{30,66,67} and are generally attributed factors like grain boundaries, grain orientations or interfacial dead zones^{68,69}. Some experimental values exceed f_{ideal} , such as with added nanoparticles⁷⁰ or using electrostatic interaction³³, and can also exceed 1 for some BCP compositions⁶⁴.

Figure 6 illustrates the morphology factor for PPIL BCPs with PIL mol% = 25, 50, and 71, corresponding to ϕ_{PIL} = 43.2, 69.5, and 85.1,

respectively (Table 1). Density of 1.28 and 1.51 g/cm³ for PBLG (from the literature⁵²) and PTPLG (determined by pycnometer), respectively, were used to calculate the volume fractions. The f values of PBLG₃₀-*b*-PTPLG₁₀ ranges from 0.005 to 0.03 and PBLG₃₀-*b*-PTPLG₃₀ ranges from 0.03 to 0.05 with temperature, all significantly lower than $f_{LAM, ideal} = 2/3$. This is likely due to the grain boundaries, coexistence of two LAM phases and poorly-ordered LAM structures as evidenced by the shoulder peak in SAXS. Interestingly, PBLG₃₀-*b*-PTPLG₇₅ gave an unexpectedly high f values ($f > 0.8$ across the entire temperature range), surpassing even $f_{LAM, ideal}$, which was attributed to the combination of higher PIL composition (71 mol %) and the formation of highly ordered bilayer LAM structures. The highly ordered ionic domains and closely packed TFSI anions in this structure create a favorable environment for ion transport with a continuous pathway, resulting in high conductivity and morphology factor. This enhancement in conductivity may be due to the alignment of peptides and the macrodipoles along the interfaces, which can enhance the local dielectric constant leading to greater ion pair dissociation and increased TFSI mobility. The helices will also have a consistent spacing of tethered cations away from the interface which can facilitate TFSI motion between helices. Additionally, the high morphology factors may also be a result of some orientation induced during processing. Future work quantifying how processing or controlled shear alignment can orient the diblocks would be helpful to understand the upper limits of conductivity in peptide-peptide systems. When normalized by ionic content, this BCP is more conductive than the corresponding homopolymer, indicating more favorable ion transport within the nanostructures. The increase in N is also a factor that enhances the strength of microphase separation and increases the normalized conductivity²⁷. Moreover, f values substantially increase as the temperature decreasing, reaching 1.3 at 40 °C. This indicates that the bilayer LAM structure enhances ion transport at lower temperatures compared to the homopolymer, offering creative insights for the design of future high-performance polymer electrolytes.

Solid-state helical-helical polypeptide polymerized ionic liquid block copolymers were investigated to determine the role of secondary structure on assembly and conductivity. PBLG₃₀-*b*-PTPLG_ns with fixed non-ionic PBLG lengths but varying ionic PTPLG length were synthesized and analyzed. The helical conformation and thermal properties were characterized by ATR-FTIR and DSC, respectively. SAXS analysis confirmed strong microphase separation in these PPIL BCPs, which self-assembled into LAM structures with varying d and degrees of order, where higher PIL mol % (and largest N) led to larger d and a higher degree of order. PBLG₃₀-*b*-PTPLG₇₅ with the longest PIL block formed a highly ordered bilayer LAM structure and exhibited a ~ 1.5 – 2 order of magnitude higher conductivity than PBLG₃₀-*b*-PTPLG₃₀ and PBLG₃₀-*b*-PTPLG₁₀ with poorly order LAM structure. More than 20-fold increase in σ_∞ of PBLG₃₀-*b*-PTPLG₇₅ indicates the enhancement of conductivity will continue to grow upon heating up to the point of degradation. These results demonstrate the critical role of highly ordered nanoscale ionic domains and connectivity in enhancing ion transport. This is further supported by $f > 0.8$ of PBLG₃₀-*b*-PTPLG₇₅, which exceeds the ideal value for LAM phases ($f_{LAM, ideal} = 2/3$), while PBLG₃₀-*b*-PTPLG₃₀ and PBLG₃₀-*b*-PTPLG₁₀ have $f < 0.05$. These insights into the structure-property relationships of helical PPIL BCPs provide a direction for optimizing ion transport and tailoring the properties of block copolymer systems using helical backbone polymers as next-generation stable, high-performance ion-conducting electrolytes. For applications in energy storage, ions, such as Li or OH will be important and understanding how other charges are impacted by the macrodipole of a helix, block copolymer assembly, and solvent will be critical for advancing peptide electrolytes.

Methods

All detailed experimental procedures and characterization of compounds can be found in the Supplementary Information.

Synthesis of poly(γ -benzyl-L-glutamate)-*b*-poly(γ -(3-chloropropyl)-L-glutamate) (PBLG₃₀-*b*-PCIPLG_ns)

Block copolypeptides PBLG₃₀-*b*-PCIPLG_ns were synthesized with PBLG₃₀-NH₂ as initiator in an emulsion system ($V_{\text{DCM}}/V_{\text{pH}=7 \text{ phosphate buffer}} = 95\%/5\%$) using 18-Crown-6 as catalyst. Such as for PBLG₃₀-*b*-PCIPLG₃₀, 4 mM 18-Crown-6 DCM solution (12 μ L, 0.048 mmol, 2 eq), pH = 7 phosphate buffer (0.66 mL), and 4 mM PBLG₃₀-NH₂ DCM solution (6 mL, 0.024 mmol, 1 eq) were mixed together, in which 100 mM CIPLG-NCA DCM solution (7.2 mL, 0.72 mmol, 30 eq) was added and then vigorously vortexed. The mixture was allowed to stir at room temperature for 24 h. After reaction, most of the water was removed via extraction from reaction mixture, that was then dried by using anhydrous sodium sulfate. After filtration, the organic phase was concentrated to 1–2 mL and then precipitated in cold hexane/ether (v/v = 1/1) twice to yield white solid (270 mg, 88%).

Morphology characterization

SAXS and WAXS experiments were conducted simultaneously using the 16ID-LiX Beamline at the National Synchrotron Light Source II where is located at the Brookhaven National Laboratory (Upton, New York). The X-ray energy was 13.5 keV. The intensity is expressed as a function of scattering vector, q defined as $\frac{4\pi}{\lambda} \sin \frac{\theta}{2}$, where θ is the scattering angle and λ is the wavelength. The data covers a q range from 0.005 to 2.5 \AA^{-1} . All samples were hot-pressed into self-standing films at 80 °C with 1.5 tons for 5 min and then annealed at 140 °C for 4 h.

Ionic conductivity measurement

Electrochemical impedance spectra were recorded on a SP-300 Potentiostat with an intermediate temperature system. All samples' preparations were conducted in a glovebox. Pre-dried polymer was placed in a hole (with a diameter 5 mm) of a Kapton spacer between two stainless-steel electrodes (with a thickness 0.5 mm), heated to 80 °C, and then pressed into a film and held for 2 h. The hot-pressed polymer film thickness was determined by the average of three measurements with a micrometer. The cell was hermetically sealed by a crimper in the glovebox using a typical coin cell assembly. The coin cell was first heated to 140 °C and equilibrated at least 4 h. The ionic conductivity over time was collected from high temperature to low temperature with a 5 °C temperature interval and a 60-min equilibration time was applied before each measurement. The applied voltage was 100 mV, and the frequency range was 10⁶ to 0.1 Hz. The impedance data was processed to make a plot of real (σ') and imaginary (σ'') conductivities versus frequency, and the ionic conductivity of polymer electrolyte was taken as the real conductivity at the $\tan(\delta) = \sigma'/\sigma''$ maximum. Each polymer electrolyte was measured with two independent samples.

Data availability

The authors declare that all data supporting the findings of this study are available within the paper and the Supplementary Information. The raw numbers for charts and graphs are available in the provided Source Data file whenever possible. All images and data are available from the corresponding author upon request. Source data are provided with this paper.

References

- Li, Q., Yan, F. & Texter, J. Polymerized and colloidal ionic liquids horizontal line syntheses and applications. *Chem. Rev.* **124**, 3813–3931 (2024).
- Arora, S. & Verma, N. A review: advancing organic electronics through the lens of ionic liquids and polymerized ionic liquids. *RSC Appl. Polym.* **2**, 317–355 (2024).
- Nie, H. et al. Light-controllable ionic conductivity in a polymeric ionic liquid. *Angew. Chem. Int. Ed.* **59**, 5123–5128 (2020).
- Zhou, T. H., Zhao, Y., Choi, J. W. & Coskun, A. Ionic liquid functionalized gel polymer electrolytes for stable lithium metal batteries. *Angew. Chem. Int. Ed.* **60**, 22791–22796 (2021).
- Ganesan, V. Ion transport in polymeric ionic liquids: recent developments and open questions. *Mol. Syst. Des. Eng.* **4**, 280–293 (2019).
- Jones, S. D. et al. Design of polymeric zwitterionic solid electrolytes with superionic lithium transport. *ACS Cent. Sci.* **8**, 169–175 (2022).
- Griffin, P. J. et al. Ion transport in cyclopropenium-based polymerized ionic liquids. *Macromolecules* **51**, 1681–1687 (2018).
- Forsyth, M., Porcarelli, L., Wang, X. E., Goujon, N. & Mecerreyes, D. Innovative electrolytes based on ionic liquids and polymers for next-generation solid-state batteries. *Acc. Chem. Res.* **52**, 686–694 (2019).
- Wang, J. R., Li, S. Q., Zhao, Q., Song, C. & Xue, Z. G. Structure code for advanced polymer electrolyte in lithium-ion batteries. *Adv. Funct. Mater.* **31**, 2008208 (2021).
- Watanabe, M. et al. Application of ionic liquids to energy storage and conversion materials and devices. *Chem. Rev.* **117**, 7190–7239 (2017).
- Deng, X. et al. Poly(ionic liquid)-coated meshes with opposite wettability for continuous oil/water separation. *Ind. Eng. Chem. Res.* **59**, 6672–6680 (2020).
- Zhang, M. M., Semiat, R. & He, X. Z. Recent advances in poly(ionic liquids) membranes for CO₂ separation. *Sep. Purif. Technol.* **299**, 121784 (2022).
- Chen, Z. et al. Boosting H₂O₂ utilization efficiency in benzene hydroxylation to phenol via isolated single VO₄ site on hydrophobic poly(ionic liquid)-derivative. *J. Chem. Eng.* **479**, 147501 (2024).
- Zhao, H. L. et al. Poly(ionic liquid)-mediated green synthesis of 3D AuPt flower-like nanoballs with composition-dependent SERS sensitivity and catalytic activity. *J. Mol. Liq.* **381**, 121823 (2023).
- Jiang, Y. J. et al. “Metaphilic” cell-penetrating polypeptide-vancomycin conjugate efficiently eradicates intracellular bacteria via a dual mechanism. *ACS Cent. Sci.* **6**, 2267–2276 (2020).
- Jiang, Y. J., Chen, Y. Y., Song, Z. Y., Tan, Z. Z. & Cheng, J. J. Recent advances in design of antimicrobial peptides and polypeptides toward clinical translation. *Adv. Drug. Deliv. Rev.* **170**, 261–280 (2021).
- Yuan, J., Soll, S., Drechsler, M., Muller, A. H. & Antonietti, M. Self-assembly of poly(ionic liquid)s: polymerization, mesostructure formation, and directional alignment in one step. *J. Am. Chem. Soc.* **133**, 17556–17559 (2011).
- Nguyen, H. D. et al. Nanostructured multi-block copolymer single-ion conductors for safer high-performance lithium batteries. *Energy Environ. Sci.* **11**, 3298–3309 (2018).
- Park, J., Staiger, A., Mecking, S. & Winey, K. I. Ordered nanostructures in thin films of precise ion-containing multiblock copolymers. *ACS Cent. Sci.* **8**, 388–393 (2022).
- Jiang, Y. V. et al. The evolution of cyclopropenium ions into functional polyelectrolytes. *Nat. Commun.* **6**, 5950 (2015).
- Li, Q. N. et al. Poly(Ionic Liquid) double-network elastomers with high-impact resistance enhanced by cation- π interactions. *Adv. Mater.* **36**, e2311214 (2024).
- Li, L. L. et al. High-toughness and high-strength solvent-free linear poly(ionic liquid) elastomers. *Adv. Mater.* **36**, e2308547 (2024).
- Liu, L. W. et al. Excellent polymerized ionic-liquid-based gel polymer electrolytes enabled by molecular structure design and anion-derived interfacial layer. *ACS Appl. Mater. Interfaces* **16**, 8895–8902 (2024).
- Schneider, Y. et al. Ionic conduction in nanostructured membranes based on polymerized protic ionic liquids. *Macromolecules* **46**, 1543–1548 (2013).

25. Peckham, T. J. & Holdcroft, S. Structure-morphology-property relationships of non-perfluorinated proton-conducting membranes. *Adv. Mater.* **22**, 4667–4690 (2010).
26. Yuan, R. et al. Ionic conductivity of low molecular weight block copolymer electrolytes. *Macromolecules* **46**, 914–921 (2013).
27. Gomez, E. D. et al. Effect of ion distribution on conductivity of block copolymer electrolytes. *Nano Lett.* **9**, 1212–1216 (2009).
28. Meek, K. M. & Elabd, Y. A. Polymerized ionic liquid block copolymers for electrochemical energy. *J. Mater. Chem. A* **3**, 24187–24194 (2015).
29. Ye, Y. S., Sharick, S., Davis, E. M., Winey, K. I. & Elabd, Y. A. High hydroxide conductivity in polymerized ionic liquid block copolymers. *ACS Macro Lett.* **2**, 575–580 (2013).
30. Weber, R. L. et al. Effect of nanoscale morphology on the conductivity of polymerized ionic liquid block copolymers. *Macromolecules* **44**, 5727–5735 (2011).
31. Choi, J. H., Ye, Y. S., Elabd, Y. A. & Winey, K. I. Network structure and strong microphase separation for high ion conductivity in polymerized ionic liquid block copolymers. *Macromolecules* **46**, 5290–5300 (2013).
32. Harris, M. A. et al. Ion transport and interfacial dynamics in disordered block copolymers of ammonium-based polymerized ionic liquids. *Macromolecules* **51**, 3477–3486 (2018).
33. Min, J. et al. Enhancing ion transport in charged block copolymers by stabilizing low symmetry morphology: Electrostatic control of interfaces. *Proc. Natl. Acad. Sci. USA* **118**, e2107987118 (2021).
34. Jung, H. Y., Kim, S. Y., Kim, O. & Park, M. J. Effect of the protogenic group on the phase behavior and ion transport properties of acid-bearing block copolymers. *Macromolecules* **48**, 6142–6152 (2015).
35. Chen, Y. Y. et al. Helical peptide structure improves conductivity and stability of solid electrolytes. *Nat. Mater.* **23**, 1539–1546 (2024).
36. Nguyen, T. P. et al. Polypeptide organic radical batteries. *Nature* **593**, 61–66 (2021).
37. Samajdar, R. et al. Secondary structure determines electron transport in peptides. *Proc. Natl. Acad. Sci. USA* **121**, e2403324121 (2024).
38. Kuo, S. W., Lee, H. F., Huang, C. F., Huang, C. J. & Chang, F. C. Synthesis and self-assembly of helical polypeptide-random coil amphiphilic diblock copolymer. *J. Polym. Sci. Part A Polym. Chem.* **46**, 3108–3119 (2008).
39. Chen, J. T., Thomas, E. L., Ober, C. K. & Mao, G. P. Self-assembled smectic phases in rod-coil block copolymers. *Science* **273**, 343–346 (1996).
40. Borsali, R., Lecommandoux, S., Pecora, R. & Benoît, H. Scattering properties of rod-coil and once-broken rod block copolymers. *Macromolecules* **34**, 4229–4234 (2001).
41. Scanga, R. A. et al. Asymmetric polymerization-induced crystallization-driven self-assembly of helical, rod-coil poly(aryl isocyanide) block copolymers. *J. Am. Chem. Soc.* **145**, 6319–6329 (2023).
42. Stupp, S. I. et al. Supramolecular materials: self-organized nanostructures. *Science* **276**, 384–389 (1997).
43. Banno, M. et al. Two-dimensional bilayer smectic ordering of rigid rod-rod helical diblock polyisocyanides. *Macromolecules* **43**, 6553–6561 (2010).
44. Vacogne, C. D., Wei, C. X., Tauer, K. & Schlaad, H. Self-assembly of alpha-helical polypeptides into microscopic and enantiomorphic spirals. *J. Am. Chem. Soc.* **140**, 11387–11394 (2018).
45. Wang, K. H., Liu, C. H., Tan, D. H., Nieh, M. P. & Su, W. F. Block sequence effects on the self-assembly behaviors of polypeptide-based penta-block copolymer hydrogels. *ACS Appl. Mater. Interfaces* **16**, 6674–6686 (2024).
46. Klok, H. A. & Lecommandoux, S. Supramolecular materials via block copolymer self-assembly. *Adv. Mater.* **13**, 1217–1229 (2001).
47. Yang, T. J. et al. Tailoring synthetic polypeptide design for directed fibril superstructure formation and enhanced hydrogel properties. *J. Am. Chem. Soc.* **146**, 5823–5833 (2024).
48. Minich, E. A., Nowak, A. P., Deming, T. J. & Pochan, D. J. Rod-rod and rod-coil self-assembly and phase behavior of polypeptide diblock copolymers. *Polymer* **45**, 1951–1957 (2004).
49. Yang, T. J. et al. Synthesis and in situ thermal induction of beta-sheet nanocrystals in spider silk-inspired copolypeptides. *J. Am. Chem. Soc.* **146**, 31849–31859 (2024).
50. Papadopoulos, P., Floudas, G., Klok, H. A., Schnell, I. & Pakula, T. Self-assembly and dynamics of poly(gamma-benzyl-L-glutamate) peptides. *Biomacromolecules* **5**, 81–91 (2004).
51. Ye, Y. S., Choi, J. H., Winey, K. I. & Elabd, Y. A. Polymerized ionic liquid block and random copolymers: effect of weak microphase separation on ion transport. *Macromolecules* **45**, 7027–7035 (2012).
52. Zhou, Q. H. et al. Synthesis and hierarchical self-assembly of rod-rod block copolymers via click chemistry between mesogen-jacketed liquid crystalline polymers and helical polypeptides. *Macromolecules* **43**, 5637–5646 (2010).
53. Zhou, F. et al. Synthesis and self-assembly of rod-rod block copolymers with different rod diameters. *Macromolecules* **46**, 8253–8263 (2013).
54. Haataja, J. S. et al. Double smectic self-assembly in block copolypeptide complexes. *Biomacromolecules* **13**, 3572–3580 (2012).
55. Papadopoulos, P. et al. Nanodomain-induced chain folding in poly(gamma-benzyl-L-glutamate)-b-polyglycine diblock copolymers. *Biomacromolecules* **6**, 2352–2361 (2005).
56. Parry, D. A. & Elliott, A. X-ray diffraction patterns of liquid crystalline solutions of poly-gamma-benzyl-L-glutamate. *Nature* **206**, 616–617 (1965).
57. Choi, U. H. et al. Dielectric and viscoelastic responses of imidazolium-based ionomers with different counterions and side chain lengths. *Macromolecules* **47**, 777–790 (2014).
58. Zhao, Q. J., Shen, C. T., Halloran, K. P. & Evans, C. M. Effect of network architecture and linker polarity on ion aggregation and conductivity in precise polymerized ionic liquids. *ACS Macro Lett.* **8**, 658–663 (2019).
59. Robinson, C. & Ward, J. C. Liquid-crystalline structures in polypeptides. *Nature* **180**, 1183–1184 (1957).
60. Stacy, E. W. et al. Fundamental limitations of ionic conductivity in polymerized ionic liquids. *Macromolecules* **51**, 8637–8645 (2018).
61. Zhao, Q. J., Bennington, P., Nealey, P. F., Patel, S. N. & Evans, C. M. Ion specific, thin film confinement effects on conductivity in polymerized ionic liquids. *Macromolecules* **54**, 10520–10528 (2021).
62. Bocharova, V. et al. Role of fast dynamics in conductivity of polymerized ionic liquids. *J. Phys. Chem. B* **124**, 10539–10545 (2020).
63. Wojnarowska, Z. et al. Effect of chain rigidity on the decoupling of ion motion from segmental relaxation in polymerized ionic liquids: ambient and elevated pressure studies. *Macromolecules* **50**, 6710–6721 (2017).
64. Evans, C. M., Sanoja, G. E., Popere, B. C. & Segalman, R. A. Anhydrous proton transport in polymerized ionic liquid block copolymers: roles of block length, ionic content, and confinement. *Macromolecules* **49**, 395–404 (2016).
65. Fan, F. et al. Ion conduction in polymerized ionic liquids with different pendant groups. *Macromolecules* **48**, 4461–4470 (2015).
66. Wanakule, N. S. et al. Ionic conductivity of block copolymer electrolytes in the vicinity of order-disorder and order-order transitions. *Macromolecules* **42**, 5642–5651 (2009).
67. Schulze, M. W., McIntosh, L. D., Hillmyer, M. A. & Lodge, T. P. High-modulus, high-conductivity nanostructured polymer electrolyte membranes via polymerization-induced phase separation. *Nano Lett.* **14**, 122–126 (2014).
68. Wagner, T. et al. Vinylphosphonic Acid Homo- and Block Copolymers. *Macromol. Chem. Phys.* **210**, 1903–1914 (2009).

69. Kumar, A., Pisula, W. & Mullen, K. Effect of humidity and temperature on proton conduction in phosphonated copolymers. *Mater. Today Commun.* **20**, 100539 (2019).
70. Villaluenga, I., Chen, X. C., Devaux, D., Hallinan, D. T. & Balsara, N. P. Nanoparticle-driven assembly of highly conducting hybrid block copolymer electrolytes. *Macromolecules* **48**, 358–364 (2015).

Acknowledgements

This work is supported by United States National Science Foundation (NSF DMR-1751291 (PIL physics) and NSF CBET-2219305 (ion transport in BCPs) to C.M.E., and DMR-2210590 (peptide processing and properties) to Y.L.). The authors acknowledge the facility and instrumental support from the Materials Research Laboratory and the SCS NMR Laboratory, University of Illinois Urbana-Champaign. The authors thank the 16ID-LiX beamline at the NSLS-II (Brookhaven National Lab) through a beamtime proposal (BAG-302208).

Author contributions

Y.C. and C.M.E. directed the projects and designed the experiments. Y.C. conceived of the block copolymer electrolyte design and synthesis. T.Y. conducted the X-ray scattering experiments. Y.C. wrote the manuscript with contributions and critical suggestions from T.Y., Y.L., and C.M.E. All authors discussed the results and commented on the manuscript.

Competing interests

The authors declare no competing interests.

Additional information

Supplementary information The online version contains supplementary material available at <https://doi.org/10.1038/s41467-025-57784-9>.

Correspondence and requests for materials should be addressed to Christopher M. Evans.

Peer review information *Nature Communications* thanks Senthil Kumar Boopathi, Darrin Pochan, and the other, anonymous, reviewer for their contribution to the peer review of this work. A peer review file is available.

Reprints and permissions information is available at <http://www.nature.com/reprints>

Publisher's note Springer Nature remains neutral with regard to jurisdictional claims in published maps and institutional affiliations.

Open Access This article is licensed under a Creative Commons Attribution-NonCommercial-NoDerivatives 4.0 International License, which permits any non-commercial use, sharing, distribution and reproduction in any medium or format, as long as you give appropriate credit to the original author(s) and the source, provide a link to the Creative Commons licence, and indicate if you modified the licensed material. You do not have permission under this licence to share adapted material derived from this article or parts of it. The images or other third party material in this article are included in the article's Creative Commons licence, unless indicated otherwise in a credit line to the material. If material is not included in the article's Creative Commons licence and your intended use is not permitted by statutory regulation or exceeds the permitted use, you will need to obtain permission directly from the copyright holder. To view a copy of this licence, visit <http://creativecommons.org/licenses/by-nc-nd/4.0/>.

© The Author(s) 2025